processes

MDPI

Article

Study on the Bubble Collapse Characteristics and Heat Transfer Mechanism of the Microchannel Reactor

Gaoan Zheng [1,*], Pu Xu [2], Tong Wang [3] and Qing Yan [4,*]

[1] School of Mechanical Engineering, Zhejiang University of Water Resources and Electric Power, Hangzhou 310018, China
[2] College of Mechanical Engineering, Zhejiang University of Technology, Hangzhou 310014, China
[3] College of Mechanical and Electrical Engineering, Jining University, Jining 273155, China
[4] School of Economics and Management, Zhejiang University of Science and Technology, Hangzhou 310023, China
* Correspondence: zhengga@zjweu.edu.cn (G.Z.); yanqingzjut@126.com (Q.Y.)

Abstract: Microreactors have the advantages of high heat and mass transfer efficiency, strict control of reaction parameters, easy amplification, and good safety performance, and have been widely used in various fields such as chip manufacturing, fine chemicals, and biomanufacturing. However, narrow microchannels in microreactors often become filled with catalyst particles, leading to blockages. To address this challenge, this study proposes a multiphase flow heat transfer model based on the lattice Boltzmann method (LBM) to investigate the dynamic changes during the bubble collapse process and temperature distribution regularities. Based on the developed three-phase flow dynamics model, this study delves into the shock dynamic evolution process of bubble collapse and analyzes the temperature distribution regularities. Then, the flow patterns under different particle density conditions are explored. The study found that under the action of shock wave, the stable structure of the liquid film of the bubble is destroyed, and the bubble deforms and collapses. At the moment of bubble collapse, energy is rapidly transferred from the potential energy of the bubble to the kinetic energy of the flow field. Subsequently, the kinetic energy is converted into pressure waves. This results in the rapid generation of extremely high pressure in the flow field, creating high-velocity jets and intense turbulent vortices, which can enhance the mass transfer effects of the multiphase flows. At the moment of bubble collapse, a certain high temperature phenomenon will be formed at the collapse, and the high temperature phenomenon in this region is relatively chaotic and random. The pressure waves generated during bubble collapse have a significant impact on the motion trajectories of particles, while the influence on high-density particles is relatively small. The results offer a theoretical basis for understanding mass transfer mechanisms and particle flow patterns in three-phase flow. Moreover, these findings have significant practical implications for advancing technologies in industrial applications, including chip manufacturing and chemical process transport.

Keywords: microchannel reactor; heat transfer mechanism; bubble collapse characteristics; energy shock

Academic Editors: Blaž Likozar and Weizhong Dai

Received: 23 October 2024
Revised: 27 December 2024
Accepted: 15 January 2025
Published: 20 January 2025

Citation: Zheng, G.; Xu, P.; Wang, T.; Yan, Q. Study on the Bubble Collapse Characteristics and Heat Transfer Mechanism of the Microchannel Reactor. *Processes* **2025**, *13*, 281. https://doi.org/10.3390/pr13010281

1. Introduction

With the rapid development of society, the energy consumption, safety, and environmental problems faced by the traditional chemical industry have become increasingly prominent, and it is increasingly important to explore more efficient, economic, and environmentally friendly response methods. Therefore, the microchemical technology came into being and quickly became a new research hotspot and development direction [1–3]. As the core of microchemical technology, microreactors have outstanding advantages such as excellent heat and mass transfer performance, high safety, convenient and continuous control, easy amplification design, and easy industrial amplification, and they have broad application prospects in chemistry, chemical industry, energy, biology, and other fields, and are considered to be one of the important ways to achieve sustainable development of the chemical industry. In microreactors, catalyst loading on the channel wall can avoid catalyst separation and recovery problems, but due to the size of the reactor, the catalyst loading area is very small. Although the packed bed microreactor can significantly increase the catalyst load area, it will lead to flow blockage and excessive pressure drop. A structured microreactor combines the advantages of a structured catalyst and microreactor and has the characteristics of large catalyst load area and small flow pressure drop. It is a promising microreactor structure. In the structured microreactor, the gas–liquid two-phase reactants flow in the pores of the structured catalyst, and there are complex and coupled multiphase flows and material transfer and transformation processes, which are closely related to the activity of the structured catalyst, gas–liquid two-phase flow, phase interface distribution, and reactor structure. A thorough understanding of the relevant mechanism and rules will help to improve the reactor performance. However, achieving fast and efficient fluid mixing in microscale operations remains challenging due to relatively low diffusion transfer rates. Therefore, it is urgent to further improve the mixing and conveying capacity of microreactors.

The gas–liquid microreactor is a microreaction device in which the gas phase reactants react in the liquid phase. Microreactors or microchannel reactors can be in close contact with the reactants and rapidly change the pressure. The increase in the specific surface area significantly improves the mass transfer efficiency. Microreactors can suppress hot spots and promote rapid cooling and heating reactions. It can precisely control the time between fluids, interface size, and interface shape, and facilitate heterogeneous catalytic reactions [4–6]. However, the performance of the microreactor is significantly affected by the internal multiphase flow, mass transfer, and transformation processes. Therefore, the phenomenon of multiphase flow and mass transfer in microchannels has become a research hotspot. In microreactor technology, fluid diffusion and mixing problems are often encountered. By effectively managing fast flows and fully mixing reactants, the speed of chemical and biological analysis is significantly accelerated, thereby increasing the overall efficiency of experiments. During the operation of the microreactor, the samples are rapidly mixed. This ensures adequate contact between samples while minimizing sample consumption, accelerating chemical reactions, and improving analytical speed and operational efficiency [7–11]. At the microscale, studying the principle of fluid mixing and developing fast and efficient mixing technology is a very valuable research field. This has a crucial impact on the design and manufacture of microfluidic devices and their effectiveness in practical applications.

Currently, research on microreactor technology has focused on both the development of channel structures and theoretical studies [12–15]. The well-designed microchannels not only reduce the workspace of micro laboratories but also significantly accelerate reaction rates within the channels, enhancing overall analytical efficiency. The small size of microchannels leads to lower flow rates, making it challenging to exhibit macroscopic turbulence characteristics at the microscale. Thus, optimizing channel structures is crucial for the performance of microreactors. Chen et al. analyzed the mixing performance of serpentine microchannels in microreactors, finding that higher Reynolds numbers lead to the generation of vortices and chaotic behavior, resulting in more efficient mixing in square wave microreactors [16]. Rahimi et al. studied the mixing rates in microreactors using ultrasonic excitation via a piezoelectric transducer, finding that microreactors subjected to ultrasound achieved significantly higher micro-mixing efficiency than those without ultrasonic excitation [17]. Mona et al. investigated the influences of ultrasonic excitation on gas–liquid flow in T-shaped microreactors, finding that ultrasound significantly improved the mass transfer coefficient, enhancing mixing and localized turbulence [18]. Dong et al. utilized ultrasonic microreactors to enhance gas–liquid mass transfer, observing that oscillations of surface waves at the gas–liquid interface increased the specific surface area. Additionally, the cavitation microflow field accelerated interface renewal, improving the individual mass transfer coefficient [19]. Zhao et al. investigated cavitation and ultrasound-assisted nitration reactions in these microreactors. They found that ultrasonic irradiation generated and violently oscillated microbubbles within the microchannels, highlighting the effectiveness of ultrasound in promoting efficient reactions in microreactors [20]. Soleymani et al. studied the fluid dynamics and mixing characteristics of T-shaped microreactors, finding that developing flow field vortices is crucial for effective mixing performance [21]. Cha et al. designed an efficient passive checkerboard mixer, enhancing mixing performance by increasing fluid interfacial area [22]. Microreactors show good processability in a series of processes such as the synthesis of inorganic and metal nanoparticles and organic compounds, and they have been flexible and controllable in the pharmaceutical and chemical industries. However, blockage of microchannels due to increased product viscosity, or prematurely precipitated products, can lead to a disruption of the continuous flow. Therefore, more research should design and manufacture microreactors with optimal channel structure, interconnections, channel size distribution, and channel volume, and reaction conditions must be carefully modified.

Microreactors enable control over the production process by enhancing flow and mixing within the channels, leading to safer, greener, and more efficient manufacturing. Current research on microreactors primarily focuses on performance comparisons and their advantages in specific applications. There is limited research on the interactions of mass transfer, heat transfer, and fluid dynamics within the channels of microreactors, as well as on the mechanisms and patterns of catalytic properties and interfacial behavior. Moreover, the strong coupling between the complex fluid flow and transfer reaction behavior limits the understanding and effective control of microreactors.

To address these issues, this paper proposes a modeling method of multiphase flow with the lattice Boltzmann method (LBM) to explore the mass transfer mechanism of bubble collapse and particle flow characteristics. Based on the mass transfer flow model, this study investigates the dynamic evolution mechanisms of the bubble collapse process and analyzes flow patterns under different particle densities. The findings provide a theoretical basis for understanding mass transfer mechanisms in three-phase flows and identifying particle flow patterns. Additionally, they offer technical support for industrial processes, including chip manufacturing and medical drug delivery.

2. LBM Theoretical Modeling

2.1. LBM Two-Phase Flow Model

The lattice Boltzmann method (LBM) play a vital role for fluid dynamics. On the macroscopic scale, the simulated transport equations are difficult to solve analytically due to complex geometric structures or boundary conditions. At the microscale, a large number of tiny particles are used to simulate the macro problem, but the position and velocity of each particle are monitored to simulate the macro problem, which greatly increases the amount of data that need to be calculated. The fundamental idea of the lattice Boltzmann method is to simplify the kinetic model to include the basic physical properties of micro or macro processes. By establishing simplified dynamics equations, it is possible to avoid solving complex dynamics equations and tracking each particle as is performed in molecular dynamics simulations. The lattice Boltzmann method has many advantages, for example, the LBM can use parallel computation to speed up the solution time in today's increasingly developed science and technology, and it is more and more favored by researchers.

The LBM uses the lattice Boltzmann equation to represent the motion and evolution process of fluid particles [23,24]. The expression is as follows:

$$f_a^k(x + e_a\delta_t, t + \delta_t) - f_a^k(x,t) = -\frac{1}{\tau_k}\left[f_a^k(x,t) - f_a^{k(eq)}(x,t)\right] \tag{1}$$

where $f(x,t)$ is the distribution function of component k at position x and time t, and τ_k is the relaxation time of the k-th component. The discrete velocities are indicated by e_α, δt is the time step, $f_k{}^{eq}$ is the equilibrium distribution function, and the discrete velocity model used is the D3Q19 model.

$$E = \begin{bmatrix} 0 & 1 & -1 & 0 & 0 & 0 & 0 & 1 & -1 & 1 & -1 & 1 & -1 & 1 & -1 & 0 & 0 & 0 & 0 \\ 0 & 0 & 0 & 1 & -1 & 0 & 0 & 1 & -1 & -1 & 1 & 0 & 0 & 0 & 0 & 1 & -1 & 1 & -1 \\ 0 & 0 & 0 & 0 & 0 & 1 & -1 & 0 & 0 & 0 & 0 & 1 & -1 & -1 & 1 & 1 & -1 & -1 & 1 \end{bmatrix} \tag{2}$$

Equilibrium distribution function of the k-th component can be given by the following [24]:

$$f_a^{k(eq)} = w_a\rho_k\left[1 + \frac{e_a \cdot u_k}{c_s^2} + \frac{(e_a \cdot u_k)^2}{2c_s^4} - \frac{{u_k}^2}{2c_s^2}\right] \tag{3}$$

where w_α is the weight coefficient, and the assigned values of 1/3 for i = 0, 1/18 for i = 1 to 6, and 1/36 for i = 7 to 18. The lattice speed of sound, c_s, is set to $\frac{1}{\sqrt{3}}$ [25,26]. The equations for density and velocity of the k-th component are defined as follows:

$$\rho_k = \sum f_a^k \tag{4}$$

$$u_k = \frac{1}{\rho_k}\sum e_a f_a^k \tag{5}$$

Assuming non-local interactions occur among different fluid particles, these interactions can be characterized by a potential energy function. This function is generally expressed in the following form [27–29]:

$$V_{kk'}(x,x') = G_{kk'}\varphi_k(x)\varphi_{k'}(x')\left(\left|x - x'\right|\right) \tag{6}$$

where $G_{kk'}(x,x')$ is the Green's function, and it indicates the strength of the interactions. The term $x' = x + e_a\delta_t$ denotes the neighboring lattice positions around x. The Green's function is defined as follows:

$$G_{kk'}\left(\left|x - x'\right|\right) = \left\{\begin{array}{cc} G & |x - x'| = \delta_x \\ 0 & |x - x'|\rangle\delta_x \end{array}\right\} \tag{7}$$

Based on the interaction potential, the interaction force between the k-th component particles and other component particles in the system can be calculated [30]. This interaction force can be described as follows:

$$F_f(x) = -G_{kk'}(x,x')\varphi_k(x)\sum_a w_a\varphi_{k'}(x + e_a\delta_t)e_a \tag{8}$$

In the contact zone between the fluid and solid interfaces, considering the wetting characteristics of the wall, the interaction force between the fluid and the solid wall can be represented via the following equation [31]:

$$F_w(x) = -\varphi_k(x)\sum_a G_w w_a s(x + e_a\delta_t)e_a \tag{9}$$

where G_w is the strength of the interaction between the fluid phase and the solid wall. The variable $s(x)$ indicates the status of the solid lattice points; if x is a solid lattice point, then $s(x) = 0$; otherwise, $s(x) = 1$. Gravity is calculated as follows:

$$F_g(x) = -\rho_k \cdot g \tag{10}$$

where g is the gravity acceleration.

2.2. DEM Model

The discrete element method (DEM) is commonly employed to tackle discontinuity problems, particularly demonstrating its unique advantages in simulating the dynamic behavior of discrete systems [32–35]. In this approach, each discrete particle is modeled as a rigid body with mass, and its translational and rotational motions adhere to Newton's second laws. The equilibrium equation for each discrete element is formulated as follows [36]:

$$M\ddot{a} + C\dot{a} + Ka = f \tag{11}$$

where a is the displacement, $\dot{a}$ is the first derivative of displacement with respect to time (velocity), $\ddot{a}$ is the second derivative of displacement with respect to time (acceleration), f is the applied load, M is the mass matrix, K is the stiffness matrix, and C is the damping matrix.

In the immersed boundary method (IBM), solid nodes are classified as internal solid nodes or boundary solid nodes, while fluid nodes are categorized into fluid boundary nodes and pure fluid nodes. The local solid fraction ϵ_s quantifies the proportion of the surrounding area covered by solid material. For pure fluid nodes, $\epsilon_s = 0$; for internal solid nodes, $\epsilon_s = 1$; and for boundary solid nodes and fluid boundary nodes, ϵ_s values range from 0 to 1 [37].

The IBM extends the traditional LBM by introducing the solid fraction ϵ_s and additional collision terms Ω_i^s. This modification facilitates a smooth transition between fluid dynamics at nodes occupied only by fluid and rigid body motion at nodes occupied exclusively by solid particles [38]. Excluding external forces, the modified lattice Boltzmann equation in the IBM framework can be described as follows:

$$f_i(x + c_i\Delta t, t + \Delta t) - f_i(x,t) = \frac{\Delta t}{\tau}(1 - B)\left[f_i^{eq}(\rho, u) - f_i(x,t)\right] + B\Omega_i^s \tag{12}$$

where Ω_i^s is the collision term, which is derived from the standard bounce-back scheme for the nonequilibrium part, and B is the weighting function that depends on the local solid fraction, with their expressions given as follows [39]:

$$B = \frac{\varepsilon_s(\tau - 0.5)}{(1 - \varepsilon_s) + (\tau - 0.5)} \tag{13}$$

$$\Omega_i^s = f_{-i}(x,t) - f_i(x,t) + f_i^{eq}(\rho, u_s) - f_{-i}^{eq}(\rho, u) \tag{14}$$

where u_s is the velocity of the solid nodes, and f_{-i} is used to denote the standard bounce-back state of f_i.

The force and torque exerted by the fluid on particles are represented by the grid nodes that cover the particles. Each node applies both a force and a torque to the particles. The total force F and torque T experienced by the solid particles are the vector sums of the forces and torques produced by all the grid nodes covering the particles, expressed as follows [40]:

$$F = \sum_{j=1}^{n} \left(B_j \sum_{i=0}^{8} \Omega_i^s c_i \right) \tag{15}$$

$$T = \sum_{j=1}^{n} \left(\left(x_j - x_p \right) B_j \sum_{i=0}^{8} \Omega_i^s c_i \right) \tag{16}$$

where n is the number of grid nodes covering the solid particles, x_j is the position vector of the j-th grid node, and x_p is the position vector of the center of the solid particle.

3. Numerical Model Experiments of Microreactor

3.1. Three-Dimensional Physical Model

The gas–liquid–solid mixing in microreactors exhibits pronounced nonlinear and chaotic behavior, characterized by complex interactions among multiple physical fields [41–44]. Therefore, understanding the dynamic processes of bubbles within microreactors and their influence on particle flow patterns is crucial. To elucidate the movement patterns of bubbles driven by fluid forces, this study establishes a 3D model for numerical simulations. Serpentine channels, due to their unique design and performance, can utilize secondary flows generated by centrifugal forces to enhance heat transfer and improve heat exchange efficiency. The serpentine channels offer significant advantages in industrial heat exchange, fluid transport, high-pressure systems, and pipeline inspections in specialized environments.

This study utilizes a microreactor with a common serpentine channel, illustrated in Figure 1, which details the specific structure and dimensions of the geometric model. To optimize the simulation time and computational efficiency, the geometric model is simplified. The pipe diameter is 2 mm, with a total length of 15 mm for the straight sections. The outer wall radius at the bends is 3 mm, while the inner wall radius is 1 mm. A bubble is placed within the pipe to simulate the flow effects of the bubble in the flow field and study the evolution of the bubble collapse process.

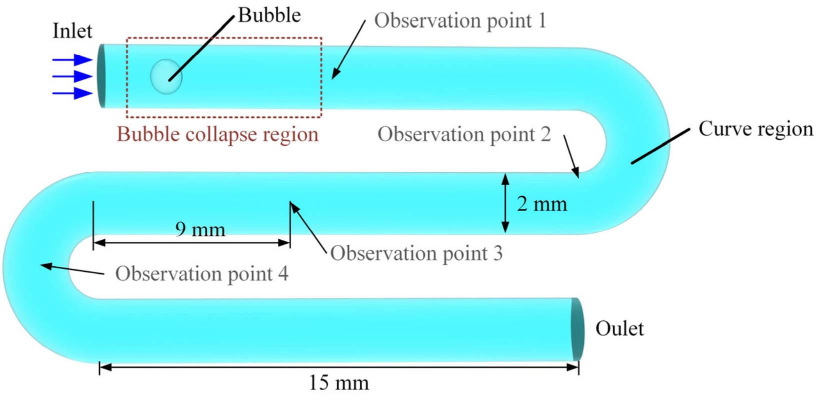

Figure 1. Three-dimensional physical model of the microchannel.

3.2. Boundary and Initial Conditions

In the numerical model, it is essential to establish boundary conditions for the fluid region to effectively solve the momentum equations of the flow field. Accurate numerical solutions can only be achieved when these boundary conditions are both scientifically sound and reflective of real-world applications [45–49]. The initial fluid domain in the fluid region module is determined using a functional form. With a bubble diameter of 1 mm positioned 1 mm from the pipe entrance, the fluid domain function is set as follows:

$$(x-0.001)^2+y^2+z^2>0.00000025 \tag{17}$$

This function indicates that a bubble with a diameter of 1 mm is located 1 mm from the entrance, and the rest of the fluid except the bubble is in the first phase. The first phase is defined as water, and the second phase is set as air. To reduce the computational demand near the wall, enhanced wall functions are used to estimate the velocity at the nearest wall. The numerical model implements a velocity inlet boundary condition, with velocities set at 1 m/s, 1.5 m/s, 2 m/s, and 2.5 m/s. The outlet is defined as a no-reflux pressure outlet boundary condition, with the outlet pressure maintained at atmospheric pressure.

In the numerical model, particle diameters are set at 0.2 mm. By simulating particles of varying densities, this study investigates the impact of bubble collapse on different particles. Three types of particle materials are selected, namely, coal powder, polystyrene beads, and polytetrafluoroethylene (PTFE) beads, with densities of 480 kg/m^3, 1050 kg/m^3, and 2200 kg/m^3. The collision model employed for the particles is the Herz–Mindlin no-slip contact model, based on the physical framework illustrated in Figure 1 and the parameters outlined in Table 1. The particles are assumed to be spherical, which facilitates the calculation of relevant properties such as mass, volume, and moment of inertia [50–55].

Table 1. Parameter settings of the numerical model.

Parameter	**Value**
Multiphase model	Particle tracking model
g (m/s^2)	−9.81
Initial distribution function in fluid domain	$(x-0.001)^2+y^2+z^2>0.00000025$
Entrance velocity (m/s)	1, 1.5, 2, 2.5
Radius of bubble (mm)	0.5
Outlet pressure	Standard atmospheric pressure
Wall function	Enhanced wall function
Particle diameter (mm)	0.2
Particle density (kg/m^3)	480, 1050, 2200

While the simplified geometric model provides a computationally efficient framework, it inherently assumes an idealized uniformity and symmetry, excluding factors such as wall roughness, localized geometric variations, and three-dimensional flow complexities. These simplifications could affect the detailed representation of flow near the boundaries and interactions in non-uniform scenarios [56–60]. However, these limitations are unlikely to significantly impact the conclusions of this study. The primary focus is on the mechanisms of bubble collapse and particle dynamics, which are largely captured by the simplified model. The symmetry assumption and exclusion of wall roughness primarily influence small-scale turbulence and flow irregularities, which have minimal effects on the overarching trends and mechanisms investigated in this work.

In simulating the motion of the particle phase, a particle tracking technique is utilized to establish a coupling mechanism between the moving boundary and accumulated variables [61–65]. This method calculates interactions among particles, as well as between the fluid and particles, across multiple physical fields. It ensures that particle sizes are smaller than the minimum grid size of the flow field numerical model while meeting the necessary accuracy for calculations [66,67].

In the multi-field coupled simulation model, a particle generator is positioned at the inlet of the pipe to produce particles. During the fluid–structure coupling simulation, the flow field solver first calculates the forces exerted by the fluid on the particles, including hydrodynamic forces and inter-particle interactions. These forces are then used to resolve the motion equations of the particles and update their positions in real time [68]. This continuous process aims to effectively track the movement paths and states of particles within the fluid.

4. Numerical Results and Analysis

4.1. Bubble Collapse Evolution Mechanism

The bubble collapse significantly influences the fluid dynamic characteristics within the flow channels, affecting parameters such as flow velocity and pressure distribution, which can alter flow patterns and overall efficiency. To investigate the impact of bubble collapse on the multiphase flow field, this study introduces a single bubble into the fluid field. This section monitors variations in velocity, pressure, turbulence intensity, and vorticity by establishing observation points within the flow field. The observation points are precisely positioned at the location of the bubble collapse to analyze the dynamic changes in the flow field in that area. Figure 2 illustrates the instantaneous pressure distribution during bubble collapse in the mixing flow field. The simulation conditions include an inlet velocity of 2.5 m/s. In the pressure contour map, darker blue indicates lower pressure values, while darker red represents higher pressure values. To accurately observe the bubble collapse state, this study selects the flow field distribution at the moment of bubble collapse (t = 0.68 ms) and the evolution process of the flow field parameters at the observation point at the bubble center, as shown in Figures 2–5.

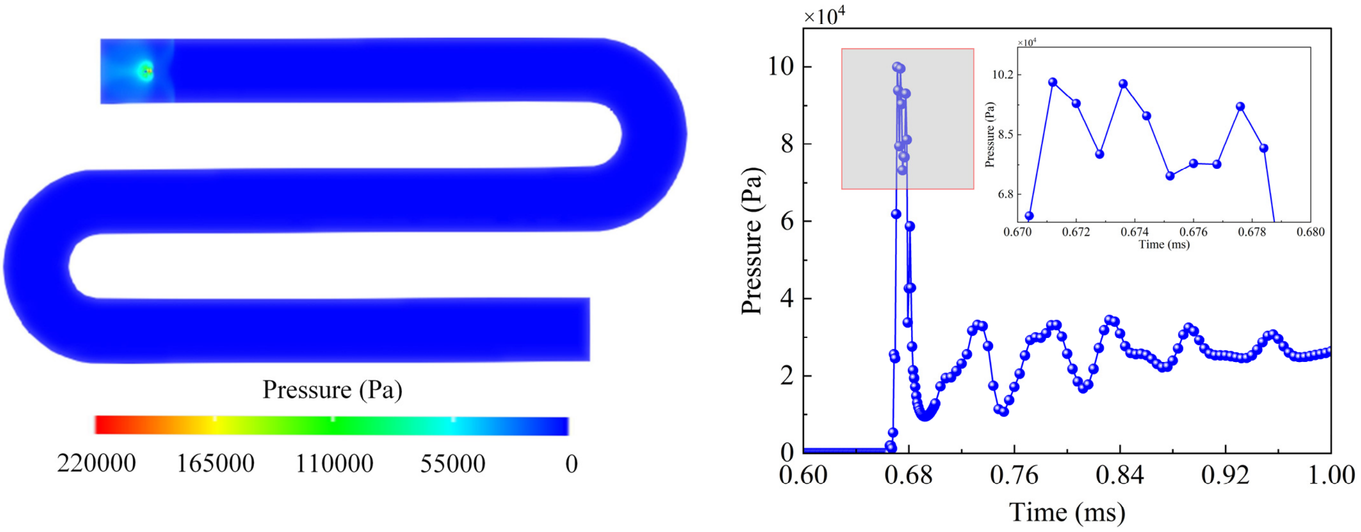

(**a**) (**b**)

Figure 2. Pressure contour and pressure curve during bubble collapse. (**a**) Pressure contour distribution during bubble collapse. (**b**) Time-varying pressure curve at the bubble collapse point.

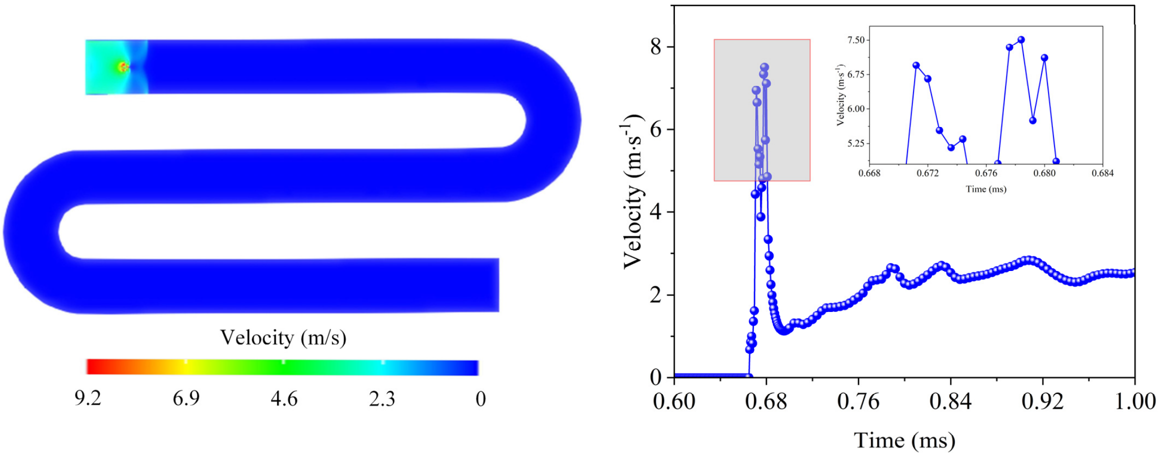

(**a**) (**b**)

Figure 3. Velocity contour and velocity curve during bubble collapse. (**a**) Velocity contour distribution during bubble collapse. (**b**) Time-varying velocity curve at the bubble collapse point.

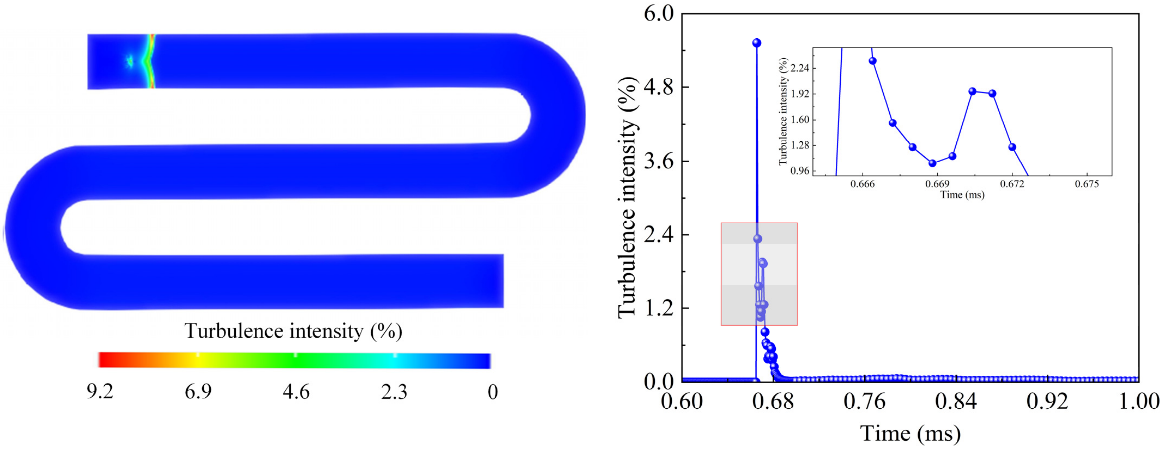

(**a**) (**b**)

Figure 4. Turbulence intensity analysis during bubble collapse. (**a**) Turbulence intensity distribution. (**b**) Turbulence intensity curve at the collapse point.

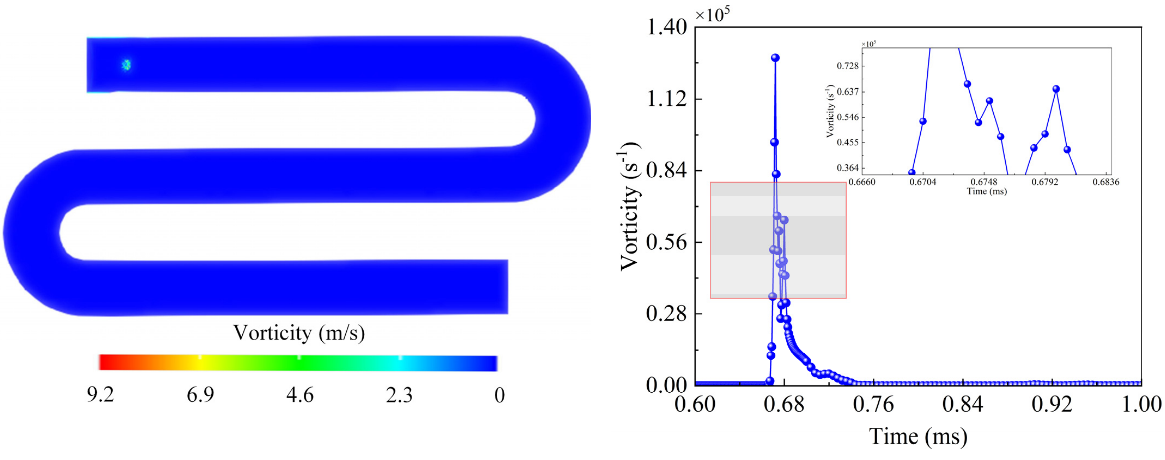

(**a**) (**b**)

Figure 5. Vorticity distribution and vorticity curve during bubble collapse in the flow field. (**a**) Vorticity distribution. (**b**) Time-varying vorticity curve.

Figure 2a shows that the bubble collapse region occupied a very limited space within the flow field, yet it exhibited a pressure level significantly higher than surrounding areas.

Figure 2b reveals that there were minor pressure fluctuations before the bubble collapsed; as the bubble moved through the flow field, the recorded pressure values dropped to 0 pa when the observation point entered the bubble. At the instant of bubble collapse, the potential energy stored in the bubble was rapidly converted into kinetic energy, generating a pressure wave, which caused the pressure in the flow field to increase dramatically in a very short time, resulting in a high-speed jet. The pressure wave was rapidly transmitted into the flow field, showing an obvious reflective pressure wave. When the bubble collapsed, the inertial effect of the surrounding liquid pushed the liquid to contract towards the center of the bubble and form a high-speed jet at the collapse point. As a result, the pressure value at the observation point rose sharply and reached 99,972 Pa at the collapse point. After the collapse, the pressure dropped rapidly and fluctuated with the dynamics. This was due to the fact that at the entrance, the pressure wave encountered the boundary and reflects, forming a fluctuating pressure field. The asymmetric nature of the bubble wall contributed to complex pressure variations during the collapse, significantly affecting the surrounding flow structure. A deeper investigation into this phenomenon will enhance the understanding and prediction of bubble collapse effects on fluid dynamics, facilitating more effective utilization and control in industrial applications.

During the bubble collapse process, the bubble experiences rapid contraction and expansion, influenced by the internal gas pressure, surface tension, and dynamic interactions with the surrounding fluid. Figure 3 illustrates the instantaneous velocity changes in the bubble in the mixing flow field during collapse, under the same conditions as the pressure maps. In Figure 3a, despite the limited area of the collapse region, the darker color indicates a significantly higher velocity compared to other parts of the flow field. This reflects a rapid conversion of the bubble's potential energy into kinetic energy, resulting in high-velocity micro-jets. Before the bubble collapsed, the recorded flow velocity at the observation point was 2.5 m/s, as shown in Figure 3b. When the observation point was inside the bubble, the recorded velocity dropped to 0 m/s. However, at the moment of bubble collapse, the velocity at the observation point sharply increased to 6.95 m/s, three times the initial velocity. After the collapse, the velocity began to decrease and fluctuated with the flow of the field. These phenomena indicate that the bubble collapse generated a strong energy shock, increasing the velocity of the surrounding fluid and forming micro-jets. These micro-jets created localized high-pressure, high-velocity regions around the bubble, thereby influencing the flow characteristics of the flow field. At the instant of bubble collapse, the flow velocity at the observation point oscillated at high speed due to the pressure wave at the instant of bubble bursting. With the time evolution, the velocity near the observation point showed obvious fluctuations under the action of the fluctuating pressure field generated by the bubble collapse. A more obvious distribution of rippled flow velocity is presented in the velocity cloud map.

Turbulence intensity is a key parameter that characterizes the turbulent state of fluid flow, reflecting the irregularity and chaotic nature of the movement. It describes a complex three-dimensional flow phenomenon in which fluid velocity, pressure, and related parameters exhibit random fluctuations over time and space. Figure 4 presents the turbulence intensity measured at the collapse point during bubble collapse. In Figure 4a, the redder color at the collapse point indicates a higher turbulence intensity compared to other areas of the flow field. The bubble underwent rapid contraction and expansion during the collapse, as described by the Rayleigh–Plesset equation. This swift movement and deformation induced turbulence in the surrounding fluid, leading to an increase in turbulence intensity. Figure 4b shows that prior to collapse, turbulence intensity was nearly zero, with little turbulence present. However, at the moment of bubble collapse, the turbulence intensity peaked at 5.51% at the collapse point. This increase in turbulence intensity enhanced the mixing process within the fluid, thereby improving mass and heat transfer efficiency. Following the collapse, the turbulence intensity at the observation point began to decrease and fluctuate with the flow. At this stage, turbulence could lead to uneven velocity distribution, potentially impacting the efficiency of fluid transport.

Vorticity describes the rotation and circulation phenomena of mixed fluids in microreactors. Figure 5 illustrates the vorticity field of the entire flow field at the moment of bubble collapse, along with the corresponding vorticity value at the collapse point. The uneven distribution of vorticity can lead to flow instability, subsequently affecting the fluid's flow state and its transition to turbulence. In Figure 5a, the stretching and bending deformation of the fluid microstructures at the moment of bubble collapse significantly influenced the distribution and intensity of the vorticity field. Several small vortices emerge at the collapse point, with the instability of the fluid flow generating and enhancing vorticity, while no vortices were observed in other areas. Figure 5b shows that before the bubble collapsed, no small vortices were formed, and the vorticity value was nearly zero. However, at the moment of collapse, numerous small vortices appeared, indicating a strong conversion of potential energy into kinetic energy, with peak vorticity reaching 127,977 s^{-1} at one of the vortices. After the bubble collapse, localized vortices persisted in the flow field; however, their vorticity values were significantly lower than the peak observed during the collapse. This behavior underscores the dynamic changes in the flow characteristics resulting from the bubble's interaction with the surrounding fluid.

The observed phenomenon indicates that the complex movement of fluid during bubble collapse led to changes in vorticity, accompanied by significant energy transitions that generated strong nonlinear characteristics within the local flow field. Due to the rapid conversion of energy from potential energy to kinetic energy during bubble collapse, which generates pressure waves, high-speed jets, and strong turbulent vortices, this property can be utilized to enhance mixing and mass transfer in microchannels. When designing microchannels, the bubble collapse mechanism can be introduced to improve the reaction efficiency. Understanding the energy evolution during this process is essential for predicting and controlling the complex behaviors, including chemical engineering, medicine, and environmental engineering. By investigating these physical mechanisms, we can enhance the design and optimization of related equipment, ultimately improving efficiency and safety.

4.2. Flow Field Temperature Distribution Patterns

To investigate the simulation of temperature variations within the microchannel, this study selected three different external ambient temperature conditions: 100 °C, 200 °C, and 300 °C. Four observation points were established inside the pipe to monitor temperature changes at key locations: at the midpoint of the inlet straight section, near the lower wall of the first bend, at the midpoint of the second straight section, and at the midpoint of the second bend. By setting up four observation points, the temperature variations in the bend and straight sections can be compared, and the relationship between the distance from the wall and the temperature rise can be analyzed. The bubble motion and collapse influence the temperature distribution of the water flow. To reveal the temperature variation patterns in the microchannel containing bubbles, this study calculates the temperature changes over time at these four observation points, as depicted in Figure 6, with temperatures measured in Kelvin (K). For reference, 0 °C is equivalent to 273.15 K, the ambient temperatures of 100 °C, 200 °C, and 300 °C convert to 373.15 K, 473.15 K, and 573.15 K, respectively, while the water temperature at 15 °C corresponds to 288.15 K. The temperature records from observation point 1 in Figure 6a indicate that the external ambient temperature had a minimal impact on the flow temperature. The bubble collapse in the fluid generated radial velocities in localized areas, and the temperature fluctuations observed at point 1 in the initial stages were a result of this bubble collapse.

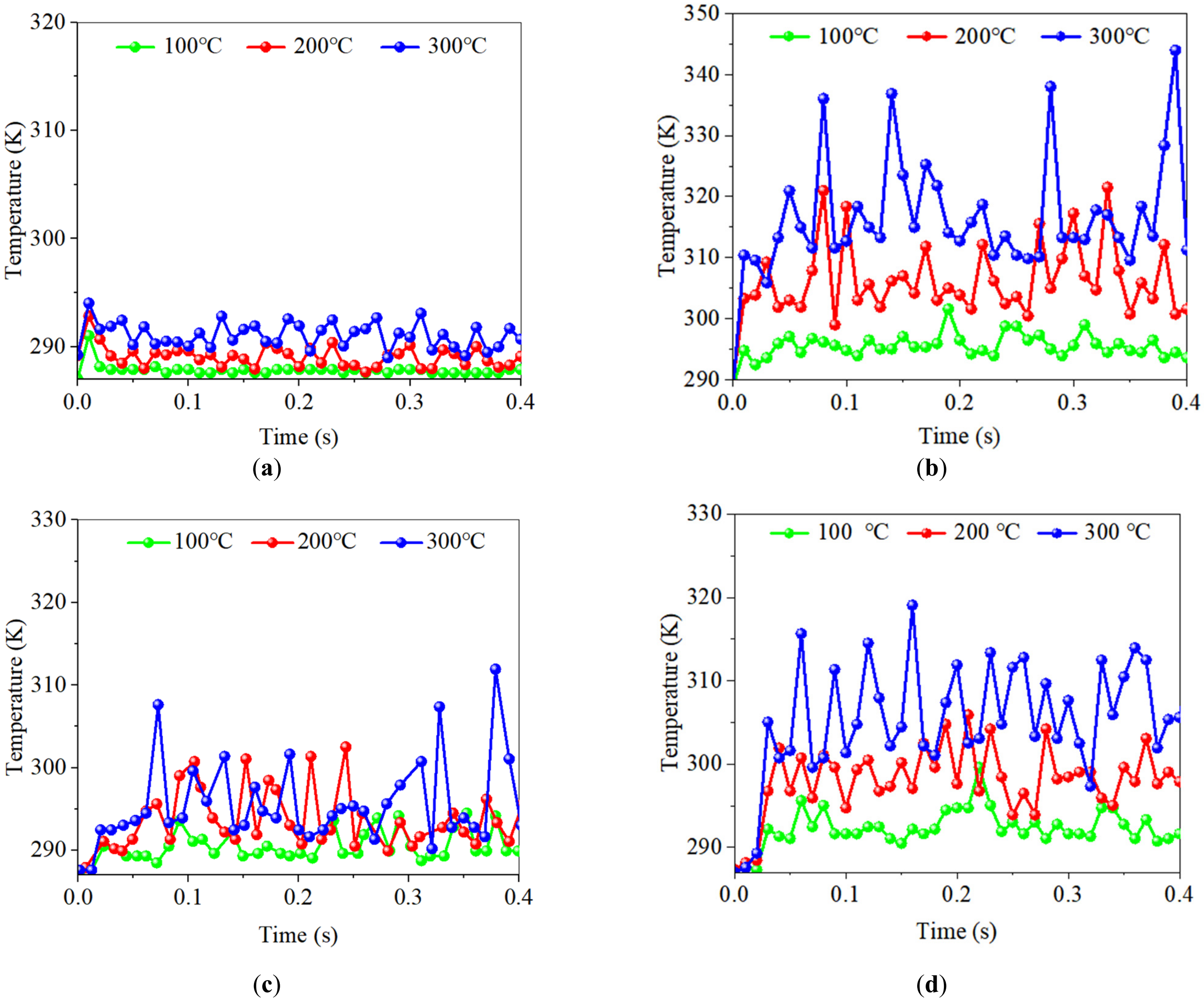

(**a**) (**b**) (**c**) (**d**)

Figure 6. Temperature distribution at observation points in the flow field. (**a**) Observation point 1. (**b**) Observation point 2. (**c**) Observation point 3. (**d**) Observation point 4.

In contrast, observation point 2, located near the pipe wall, was more affected by the external ambient temperature. As shown in Figure 6b, the temperature values at this point fell between the initial water temperature and the external ambient temperature. The increased turbulence and frequent bubble collapses in the initial part of the bend led to noticeable temperature variations at point 2 under different ambient conditions. Higher temperature environments typically result in greater fluctuations; for instance, at an ambient temperature of 573.15 K, the temperature at observation point 2 peaked at 345 K. This rise was attributed to the enhanced radial temperature gradient within the pipe under elevated temperature conditions. Comparing Figure 6a,c, it is evident that the temperature at observation point 3 consistently exceeded that at observation point 1 across all ambient temperature conditions. This suggests that the bend facilitates mixing between the fluid at the pipe center, enhancing overall temperature distribution.

Observation point 4, located in the bend region where radial fluid flow is more pronounced, maintained a higher temperature than observation point 3, as illustrated in Figure 6c,d. While both points were situated at the center of the pipe, their temperatures were lower than that of observation point 2, which was closer to the wall. The presence of the bend caused temperatures at points 3 and 4 to exhibit irregular fluctuations. These findings indicate that the temperature increased the closer one was to the wall, aligning more closely with the external ambient temperature. In the center of the flow field before entering the bend, temperatures were nearly unaffected by external environmental conditions; however, the collapse of the bubble led to localized temperature increases. The temperature of the flow field in the center of the pipe changed after passing through the bend, as seen at observation points 1, 3, and 4. Observation point 3, which experienced a bend, had a temperature that was noticeably higher than that of observation point 1, also located in the middle of a straight section. Meanwhile, observation point 4 began to be influenced by the second bend after passing through the first, resulting in a temperature higher than that of observation point 3. Overall, the temperature within the flow field showed irregular variations due to the effects of the bends and bubble collapse, leading to an increase in the central temperature and creating a more uniform overall temperature distribution.

To observe temperature changes within the flow channel more clearly, this study simulated temperature variations in the pipe before and after bubble collapse under an ambient temperature of 573.15 K and an initial water temperature of 288.15 K, as depicted in Figure 7. The flow velocity in the simulation was set at 2.5 m/s, considering a single bubble. The temperatures shown in the figure are in Kelvin. Since the high ambient temperature of 573.15 K only affects the pipe's exterior, the actual internal temperature, influenced by the water temperature, could not reach 573.15 K but could only approach it. Figure 7a illustrates that at the moment of bubble collapse, localized high-temperature regions emerged, displaying an irregular distribution. Figure 7b reveals that as the fluid flowed through the bend, periodic temperature fluctuations occurred. These observations confirm several key conclusions: the temperature near the wall is higher than that in the central region, the local temperature in the bubble collapse area exceeds that of the surrounding fluid, and the overall temperature increases in the mid-bend and downstream flow field. By adjusting the timing of bubble generation and collapse, the hydrodynamic properties and temperature transfer can be more effectively controlled.

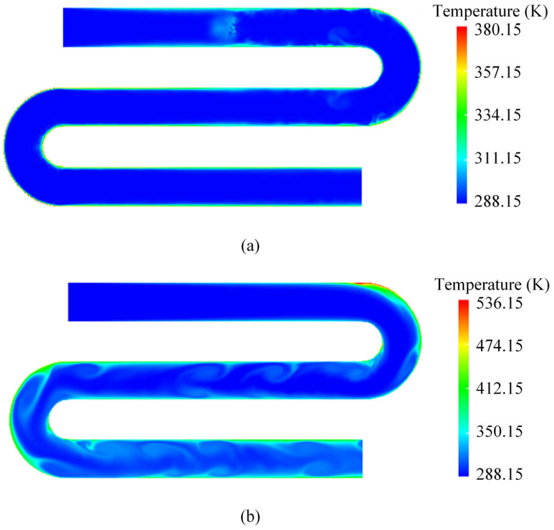

Figure 7. Temperature evolution contour of the flow field before and after bubble collapse. (**a**) Before bubble collapse. (**b**) After bubble collapse.

4.3. Particle Motion Patterns

The motion of particles refers to the movement of solid particles suspended in a fluid as they are carried along by the flow. This study explores the flow characteristics of particles within a mixing flow field, specifically examining the dynamics of a single particle influenced by a single bubble. Figure 8 illustrates the evolution of the bubble. The particle diameter was set at 0.2 mm, with an inlet flow velocity of 1 m/s. As the flow drove the bubble forward, it gradually decreased in volume until it collapsed. At the moment of collapse, the bubble generated a significant pressure wave that peaked shortly after bursting, greatly affecting particle motion. This phenomenon demonstrates that the micro-jets and pressure waves created during bubble collapse can considerably enhance particle dynamics, subjecting them to substantial forces that alter their trajectories and distribution within the fluid. Such enhanced particle motion may impact the overall flow characteristics of the fluid, as well as the efficiency of mass transfer.

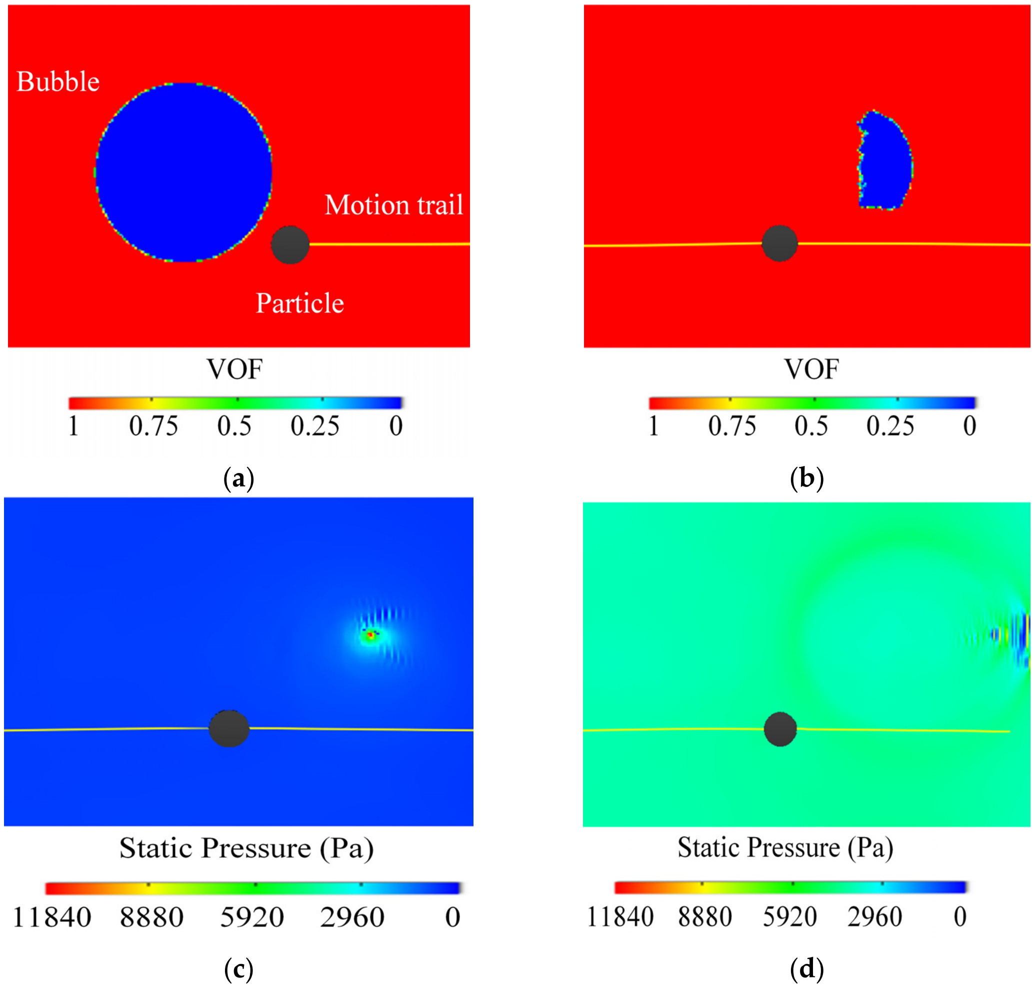

(**a**) (**b**) (**c**) (**d**)

Figure 8. Dynamic process of bubble collapse in the flow field. (**a**) t = 0 ms. (**b**) t = 2.7 ms. (**c**) t = 3.1 ms. (**d**) t = 3.38 ms.

Figure 8 illustrates the evolution process of the interaction between a single particle and a single bubble within the flow field. In Figure 8a, the bubble is represented in blue, the fluid domain in red, and the particle in black, with the particle's trajectory indicated by yellow lines. In the initial state, the bubble diameter was 1 mm, the particle diameter was 0.2 mm, and the particle was positioned at the lower right side of the bubble. As time progressed to 2.7 ms, shown in Figure 8b, the bubble began to deform and gradually shrink due to the speed effect of the inlet flow. The particle, being of greater density, lags behind the bubble in its movement. Further observations reveal that at 3.1 ms, depicted in Figure 8c, the bubble collapsed due to continued shrinking. At the moment of collapse, a significant instantaneous pressure was generated, typically exceeding the normal pressure in the flow field and reaching a peak value. In Figure 8d, as the flow field continued to move, the pressure generated from the collapse began to decrease, forming a circular pressure wave centered around the collapse point. This pressure wave expanded outward, with its diameter increasing with distance and the pressure gradually diminishing until it equilibrated with the flow field pressure. The resulting pressure wave influenced the particle's motion trajectory within the flow field, with the extent of this change depending on the particle's density.

The influence of pressure waves generated by bubble collapse varies with particle density. By setting particle densities at 480 kg/m^3, 1050 kg/m^3, and 2200 kg/m^3, we observed the impact of pressure waves generated by bubble collapse on particles of different densities. Figure 9 illustrates the motion trajectories of four types of particles influenced by the pressure waves formed during bubble collapse. At 3.25 ms, the particles were affected by the pressure waves resulting from the bubble burst, leading to changes in their motion trajectories. The impact of bubble collapse on the trajectories of the particles varied with fluid flow and particle density, indicating that as the fluid flowed, the influence of the bubble collapse on particle paths also differed according to their densities.

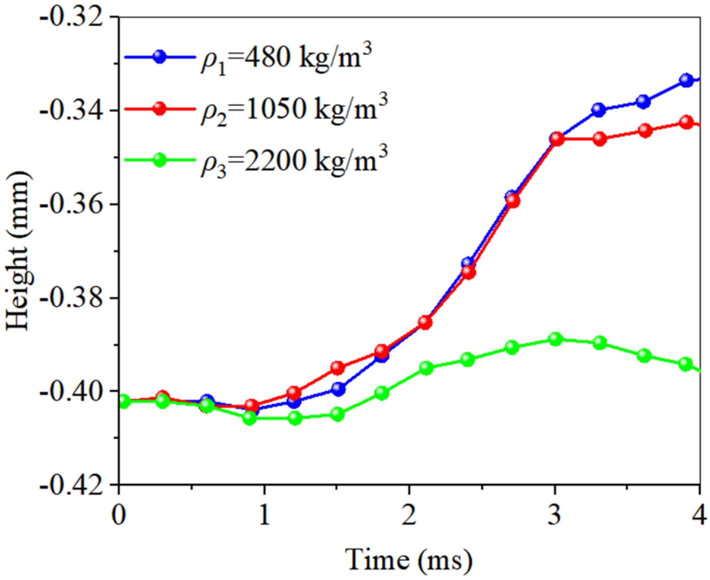

Figure 9. Motion trajectories of particles affected by bubble collapse.

To investigate the impact of the flow field in the bend region on particles with different densities, the velocity variation trends in different directions were explored, as shown in Figure 10. Before the bubble collapsed, particles with densities of 480 kg/m^3 and 1050 kg/m^3, being lower than or comparable to the density of water, exhibited relatively smooth motion trajectories and displayed some buoyant rising characteristics. However, after the bubble collapsed, the pressure wave generated from the collapse influenced the motion trajectories of both types of particles at 3.25 ms. This pressure wave temporarily interrupted the rising trend of the particles, causing them to experience a slight descent. As the pressure wave weakened, both types of particles gradually resumed their ascent. Due to the density difference, the 480 kg/m^3 particles showed a more pronounced buoyancy effect compared to the 1050 kg/m^3 particles.

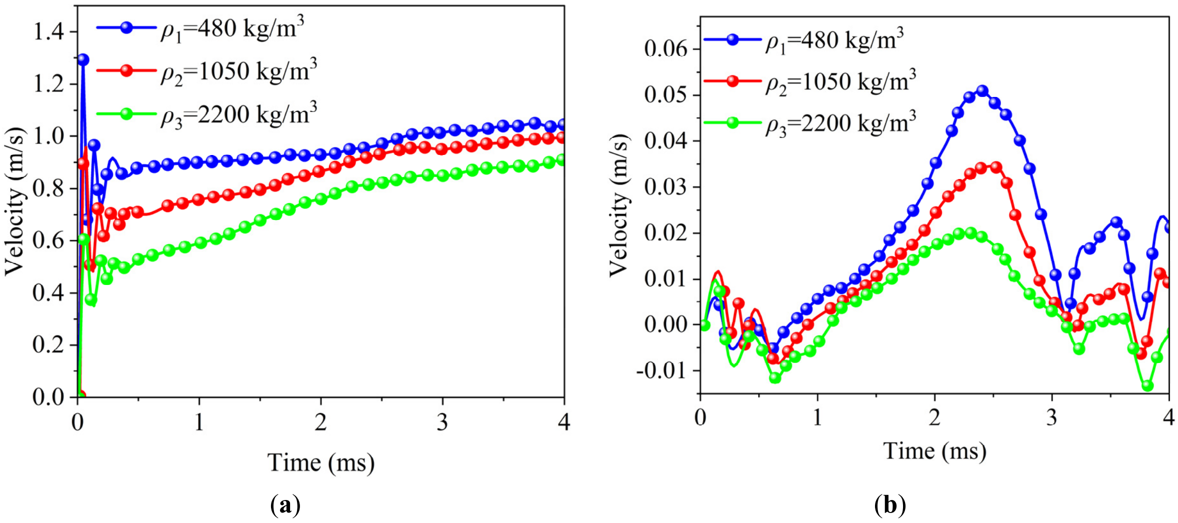

Figure 10. Variations in particle velocity in the flow field. (**a**) Changes in particle velocity in the *X* direction. (**b**) Changes in particle velocity in the *Y* direction.

In contrast, particles with a density of 2200 kg/m^3 initially tended to sink due to their greater density. Just before the bubble collapsed, however, the negative pressure region surrounding the bubble attracted these particles. When the pressure wave reached them, they continued to move downward, and this tendency became more pronounced with increasing particle density. Additionally, differences in particle densities affected their movement distances under the same flow velocity. In the simulation, high-density particles typically moved slower than low-density particles, making them less affected by the pressure wave as they remained farther from the bubble. This highlights that, under consistent external conditions, particle density significantly influences motion trajectories and responses.

The interaction between the bubble and a single particle in the flow field significantly influences particle behavior. While previous studies have examined the effect of bubble collapse on particle trajectories, a thorough analysis of the specific velocity changes in particles has been lacking. To better understand how bubble movement and collapse impact particle velocities, we monitored temporal changes in particle speed. Figure 10 presents the variations in velocity in the X and Y directions for different particle densities within the flow field. In Figure 10a, it is evident that the average velocity of particles with a density of 480 kg/m^3 in the X direction was higher than that of the other densities, aligning with the movement characteristics of lighter density particles. Around 2.5 ms, these particles experienced a slight decrease in velocity in the X direction due to the influence of the bubble. In contrast, the other particles, particularly the denser ones, were less affected by the bubble collapse and even show an increase in their X-direction velocity afterward. Figure 10b illustrates the changes in particle velocity in the Y direction. Similarly, particles with a density of 480 kg/m^3 exhibited faster velocities, while those with a density of 2200 kg/m^3 move more slowly. At approximately 2.5 ms, a significant change in velocity occurred for all particles in the Y direction, with the magnitude of change decreasing as density increased. By around 3.0 ms, the bubble collapse process was nearly complete, after which the particles began to regain speed in the Y direction, exhibiting gradual oscillations.

The above results indicate that the force received at the moment of bubble collapse can be effectively regulated by changing the density of the altered particles, which introduces a new direction for the design and regulation of microreactors.

5. Conclusions

Investigating bubble collapse characteristics and the heat transfer mechanism of the microchannel reactor is crucial for enhancing the performance of microfluidic chips and medical drug delivery. This paper proposes a modeling method for multiphase flow based on the LBM to investigate the dynamic evolution characteristics of bubble collapse process.

(1) A multiphase flow dynamics model for microreactors is developed using the LBM to explore the evolution of bubbles. The findings indicate that at the moment of bubble collapse, potential energy is converted into the kinetic energy of the flow field, which then generates pressure waves. This process results in the rapid creation of high pressure, leading to the high-velocity jets and intense turbulent vortices.

(2) In the flow field, the temperature closer to the wall is higher and approaches the external environment temperature. The temperature in the center of the flow field, which has not passed through a bend, is almost unaffected by the external environment temperature; however, the bubble collapse creates localized high-temperature phenomena, which are somewhat chaotic and random.

(3) The motion of a single bubble and a single particle shows that the bubble gradually deforms and shrinks, ultimately leading to collapse. The pressure wave generated at the moment of bubble collapse expands outward, affecting the motion trajectories of the particles. Smaller density particles are more significantly influenced by the pressure wave, resulting in larger changes in their trajectories. In contrast, higher-density particles, situated farther from the bubble, experience less impact compared to their lower-density counterparts.

In the future research, we will further develop the current coupled model based on the study in this paper to obtain more accurate motion laws of the particles in the flow field. At the same time, we will build a flow field-particle experimental platform to observe the jet phenomenon and the evolution law of particles during bubble collapse, and further develop the monitoring and control techniques for different particle parameters.

Author Contributions: Conceptualization, G.Z. and Q.Y.; tables and figures generation; writing—original draft preparation, G.Z.; funding acquisition, G.Z.; article identification, selection, and analysis, Q.Y.; review and editing, Q.Y., P.X., T.W. and G.Z.; formal analysis and investigation, G.Z. All authors have read and agreed to the published version of the manuscript.

Funding: This research received no external funding.

Data Availability Statement: The original contributions presented in the study are included in the article, further inquiries can be directed to the corresponding authors.

Conflicts of Interest: The authors declare that they have no conflicts of interest.

References

1. Gao, Z.W.; Li, C.X.; Qi, X.Y. Flow analysis on carbonaceous deposition of heavy oil droplets and catalyst particles for coking formation process. *Energy* **2022**, *260*, 124988. [CrossRef]
2. Thiebaut, M.; Quillien, N.; Maison, A. Investigating the flow dynamics and turbulence at a tidal-stream energy site in a highly energetic estuary. *Renew. Energy* **2022**, *195*, 252–262. [CrossRef]
3. Afra, B.; Karimnejad, S.; Delouei, A.A.; Tarokh, A. Flow control of two tandem cylinders by a highly flexible filament: Lattice spring IB-LBM. *Ocean Eng.* **2022**, *250*, 111025. [CrossRef]
4. Huang, X.; Xia, S.; Lee, S.; Jia, Y.; Chen, Z.; Xu, J. Continuous production of monodisperse silver nanoparticles suitable for catalysis in a droplet-based microreactor system. *ACS Appl. Nano Mater.* **2023**, *6*, 8574–8583. [CrossRef]
5. Wang, J.L.; Zhao, W.; Su, Z.; Zhang, G.J.; Li, P.; Yurchenko, D. Enhancing vortex-induced vibrations of a cylinder with rod attachments for hydrokinetic power generation. *Mech. Syst. Signal Process.* **2020**, *145*, 106912. [CrossRef]
6. Li, L.; Yang, Y.S.; Xu, W.X.; Lu, B.; Gu, Z.H.; Yang, J.G.; Tan, D.P. Advances in the multiphase vortex-induced vibration detection method and its vital technology for sustainable industrial production. *Appl. Sci.* **2022**, *12*, 8538. [CrossRef]
7. Delouei, A.A.; Karimnejad, S.; He, F.L. Direct Numerical simulation of pulsating flow effect on the distribution of non-circular particles with increased levels of complexity: IB-LBM. *Comput. Math. Appl.* **2022**, *121*, 115–130. [CrossRef]

8. Lin, H.; Shen, Q.; Ma, M.; Ji, R.; Guo, H.; Qi, H.; Xing, W.; Tang, H. 3D printing of porous ceramics for enhanced thermal insulation properties. *Adv. Sci.* **2024**, e2412554. [CrossRef] [PubMed]
9. Gu, Y.H.; Zheng, G.A. Investigate on the fluid dynamics and heat transfer behavior in an automobile gearbox based on the LBM-LES model. *Lubricants* **2025**, *in press*.
10. Škerlavaj, A.; Škerget, L.; Ravnik, J. Predicting Free–Surface Vortices with Single-Phase Simulations. *Eng. Appl. Comp. Fluid Mech.* **2014**, *8*, 193–210. [CrossRef]
11. Li, L.; Xu, P.; Xu, W.X.; Lu, B.; Wang, C.Y.; Tan, D.P. Multi-field coupling vibration patterns of the multiphase sink vortex and distortion recognition method. *Mech. Syst. Signal Process.* **2024**, *219*, 111624. [CrossRef]
12. Yang, X.; Song, F.; Zhang, T.C.; Yao, X.L.; Wang, W.L.; Zhang, Z.V.; Hou, Y.Y.; Qi, H.; Tang, H.P. Surface enhancement by micro-arc oxidation induced TiO_2 ceramic coating on additive manufacturing Ti-6Al-4V. *Chin. J. Mech. Eng.* **2024**, *in press*.
13. Ge, J.Q.; Lin, Y.H.; Qi, H.; Li, Y.T.; Li, X.L.; Li, C.; Li, Z.A.; Xu, K.Q. The impact of ultrasonic-induced jet morphology on polishing efficiency. *Int. J. Mech. Sci.* **2024**, *284*, 109764. [CrossRef]
14. Burlon, A.; Failla, G. On the dynamics of high-order beams with vibration absorbers. *Appl. Math. Model.* **2022**, *112*, 341–357. [CrossRef]
15. Li, L.; Xu, W.X.; Tan, Y.F.; Yang, Y.S.; Yang, J.G.; Tan, D.P. Fluid-induced vibration evolution mechanism of multiphase free sink vortex and the multi-source vibration sensing method. *Mech. Syst. Signal Process.* **2023**, *189*, 110058. [CrossRef]
16. Chen, X.; Li, T.; Zeng, H.; Hu, Z.; Fu, B. Numerical and experimental investigation on micromixers with serpentine microchannels. *Int. J. Heat Mass Transf.* **2016**, *98*, 131–140. [CrossRef]
17. Rahimi, M.; Aghel, B.; Hatamifar, B.; Akbari, M.; Alsairafi, A. CFD modeling of mixing intensification assisted with ultrasound wave in a T-type microreactor. *Chem. Eng. Process. Process Intensif.* **2014**, *86*, 36–46. [CrossRef]
18. Akbari, M.; Rahimi, M.; Faryadi, M. Gas–liquid flow mass transfer in a T-shape microreactor stimulated with 1.7 MHz ultrasound waves. *Chin. J. Chem. Eng.* **2017**, *25*, 1143–1152. [CrossRef]
19. Dong, Z.; Yao, C.; Zhang, Y.; Chen, G.; Yuan, Q.; Xu, J. Hydrodynamics and mass transfer of oscillating gas-liquid flow in ultrasonic microreactors. *AIChE J.* **2016**, *62*, 1294–1307. [CrossRef]
20. Zhao, S.N.; Yao, C.Q.; Zhang, Q. Acoustic cavitation and ultrasound-assisted nitration process in ultrasonic microreactors: The effects of channel dimension, solvent properties and temperature. *Chem. Eng. J.* **2019**, *374*, 68–78. [CrossRef]
21. Soleymani, A.; Kolehmainen, E.; Turunen, I. Numerical and experimental investigations of liquid mixing in T-type micromixers. *Chem. Eng. J.* **2008**, *135*, 219–228. [CrossRef]
22. Cha, J.; Kim, J.; Ryu, S.K.; Park, J.; Jeong, Y.; Park, S. A highly efficient 3D micromixer using soft PDMS bonding. *J. Micromechanics Microengineering* **2006**, *16*, 1778. [CrossRef]
23. Qiao, Z.; Yang, X.; Zhang, Y. A free-energy based multiple-distribution-function lattice Boltzmann method for multi-component and multi-phase flows. *Appl. Therm. Eng.* **2024**, *257*, 124241. [CrossRef]
24. Molaeimanesh, G.R.; Googarchin, H.S.; Moqaddam, A.Q. Lattice Boltzmann simulation of proton exchange membrane fuel cells–A review on opportunities and challenges. *Int. J. Hydrogen Energy* **2016**, *41*, 22221–22245. [CrossRef]
25. Kou, J.; Sun, S. Thermodynamically consistent modeling and simulation of multi-component two-phase flow with partial miscibility. *Comput. Methods Appl. Mech. Eng.* **2018**, *331*, 623–649. [CrossRef]
26. Guo, Q.; Cheng, P. Direct numerical simulations of sessile droplet evaporation on a heated horizontal surface surrounded by moist air. *Int. J. Heat Mass Transf.* **2019**, *134*, 828–841. [CrossRef]
27. Li, L.; Zhang, D.; Su, Y.; Hao, Y.; Zhang, X.; Huang, Z.; Zhang, W. Investigation of oil/water two-phase flow behavior in laminated shale porous media considering heterogeneous structure and fluid-solid interaction. *Phys. Fluids* **2024**, *36*, 3. [CrossRef]
28. Singh, N.K.; Premachandran, B. Coupled level set and volume of fluid method on unstructured grids for the direct numerical simulations of two-phase flows including phase change. *Int. J. Heat Mass Transf.* **2018**, *122*, 182–203. [CrossRef]
29. Wang, H.; Wang, W.; Su, Y.; Jin, Z.H. Lattice Boltzmann model for oil/water two-phase flow in nanoporous media considering heterogeneous viscosity, liquid/solid, and liquid/liquid slip. *SPE J.* **2022**, *27*, 3508–3524. [CrossRef]
30. Tashakori, A.F. Effect of inter-particle forces on solids mixing in fluidized beds. *Powder Technol.* **2023**, *415*, 118098. [CrossRef]
31. Tan, Y.F.; Ni, Y.S.; Wu, J.F.; Li, L.; Tan, D.P. Machinability evolution of gas–liquid-solid three-phase rotary abrasive flow finishing. *Int. J. Adv. Manuf. Technol.* **2023**, *131*, 2145–2164. [CrossRef]
32. Ezure, T.; Ito, K.; Tanaka, M.; Ohshima, H.; Kameyama, Y. Experiments on gas entrainment phenomena due to free surface vortex induced by flow passing beside stagnation region. *Nucl. Eng. Des.* **2019**, *350*, 90–97. [CrossRef]
33. Li, Z.; Wang, C.Y.; Li, L.; Wu, J.F.; Yin, Z.C.; Tan, D.P. Numerical investigation of mesoscale multiphase mass transport mechanism in fibrous porous media. *Eng. Appl. Comput. Fluid Mech.* **2024**, *18*, 2363246. [CrossRef]
34. Guo, X.M.; Yang, M.Y.; Li, F.Q.; Zhu, Z.C.; Cui, B.L. Investigation on Cryogenic Cavitation Characteristics of an Inducer Considering Thermodynamic Effects. *Energies* **2024**, *17*, 3627. [CrossRef]
35. Chirathalattu, A.T.; Santhosh, B.; Bose, C.; Philip, R.; Balaram, B. Passive suppression of vortex-induced vibrations using a nonlinear energy sink-Numerical and analytical perspective. *Mech. Syst. Signal Process.* **2023**, *182*, 109556. [CrossRef]

36. Tamburini, A.; Cipollina, A.; Micale, G. CFD simulations of dense solid-liquid suspensions in baffled stirred tanks: Prediction of the minimum impeller speed for complete suspension. *Chem. Eng. J.* **2012**, *193*, 234–255. [CrossRef]
37. Tao, S.; He, Q.; Yang, X.; Luo, J.; Zhao, X. Numerical study on the drag and flow characteristics of porous particles at intermediate Reynolds numbers. *Math. Comput. Simul.* **2022**, *202*, 273–294. [CrossRef]
38. Qian, Y.; Cai, R.; Zhang, L. A spheropolyhedral-based discrete elem.ent lattice Boltzmann method for simulation of non-spherical adhesive particulate flow. *Comput. Phys. Commun.* **2023**, *291*, 108809. [CrossRef]
39. Li, L.; Tan, Y.F.; Xu, W.X.; Ni, Y.S.; Yang, J.G.; Tan, D.P. Fluid-induced transport dynamics and vibration patterns of multiphase vortex in the critical transition states. *Int. J. Mech. Sci* **2023**, *252*, 108376. [CrossRef]
40. Li, L.; Lu, B.; Xu, W.X.; Wang, C.Y.; Wu, J.F.; Tan, D.P. Dynamic behaviors of multiphase vortex-induced vibration for hydropower energy conversion. *Energy* **2024**, *308*, 132897. [CrossRef]
41. Blais, B.; Bertrand, F. CFD-DEM Investigation of viscous solid-liquid mixing: Impact of particle properties and mixer characteristics. *Chem. Eng. Res. Des.* **2017**, *118*, 270–285. [CrossRef]
42. Wu, J.F.; Li, L.; Li, Z.; Xu, P.; Qi, H.; Wang, C.Y.; Zhang, Y.K.; Xie, Y.S.; Tan, D.P. Multiphase dynamic interfaces and abrasive transport dynamics for abrasive flow machining in shear thickening transition states. *Powder Technol.* **2024**, *446*, 120150. [CrossRef]
43. Xu, W.X.; Xu, P.; Yang, Y.; Tan, D.P.; Li, L. The utilization and advancement of laser ultrasound testing in the assessment of aerospace composite characteristics: A review. *Chin. J. Aeronaut.* **2025**, *in press*.
44. Stroh, A.; Daikeler, A.; Nikku, M. Coarse grain 3D CFD-DEM simulation and validation with capacitance probe measurements in a circulating fluidized bed. *Chem. Eng. Sci.* **2019**, *196*, 37–53. [CrossRef]
45. Li, L.; Li, Q.H.; Ni, Y.S.; Wang, C.Y.; Tan, Y.F.; Tan, D.P. Critical penetrating vibration evolution behaviors of the gas-liquid coupled vortex flow. *Energy* **2024**, *292*, 130236. [CrossRef]
46. Tan, Y.F.; Ni, Y.S.; Xu, W.X.; Xie, Y.S.; Li, L.; Tan, D.P. Key technologies and development trends of the soft abrasive flow finishing method. *J. Zhejiang Univ. Sci. A* **2023**, *24*, 1043–1064. [CrossRef]
47. He, L.; Liu, Z.; Zhao, Y. Study on a semi-resolved CFD-DEM method for rod-like particles in a gas-solid fluidized bed. *Particuology* **2024**, *87*, 20–36. [CrossRef]
48. Wang, C.Y.; Li, Z.; Xu, P.; Hou, Y.Q.; Tan, D.P.; Li, L. Collision modelling approach and transient response mechanism of ring-ribbed cylindric shells for underwater vehicles. *Appl. Math. Model.* **2025**, *141*, 115923. [CrossRef]
49. Li, L.; Gu, Z.H.; Xu, W.X.; Tan, Y.F.; Fan, X.H.; Tan, D.P. Mixing mass transfer mechanism and dynamic control of gas-liquid-solid multiphase flow based on VOF-DEM coupling. *Energy* **2023**, *272*, 127015. [CrossRef]
50. Li, L.; Lu, B.; Xu, W.X.; Gu, Z.H.; Yang, Y.S.; Tan, D.P. Mechanism of multiphase coupling transport evolution of free sink vortex. *Acta Phys Sin* **2023**, *72*, 034702. [CrossRef]
51. Zhang, Y.K.; Li, Z.; Li, L.; Wang, C.Y.; Wu, J.F.; Xie, Y.S.; Yin, Z.C.; Tan, D.P. Deposition mechanism of microscopic impacting droplets on flexible porous substrates. *Int. J. Mech. Sci.* **2025**, *in press*.
52. Li, L.; Xu, P.; Li, Q.H.; Yin, Z.C.; Zheng, R.Y.; Wu, J.F.; Bao, J.J.; Qi, H.; Tan, D.P. Multi-field coupling particle flow dynamic behaviors of the microreactor and ultrasonic control method. *Powder Technol.* **2025**, *in press*.
53. Xu, P.; Li, Q.H.; Wang, C.Y.; Li, L.; Tan, D.P.; Wu, H.P. Interlayer healing mechanism of multipath deposition 3D printing models and interlayer strength regulation method. *J. Manuf. Process.* **2025**, *in press*.
54. Zheng, G.A.; Weng, X.X.; Wang, T.; Xu, P.; Xu, W.X.; Li, L.; Xu, X.F.; Tan, D.P. Piezoelectric ultrasonic coupling-based polishing of micro-tapered holes with abrasive flow. *J. Zhejiang Univ.-Sci. A* **2025**, *in press*.
55. Lungu, M.; Siame, J.; Mukosha, L. Comparison of CFD-DEM and TFM approaches for the simulation of the small scale challenge problem. *Powder Technol.* **2020**, *378*, 85–103. [CrossRef]
56. Chelton, D.B.; Gaube, P.; Schlax, M.G.; Early, J.J.; Samelson, R.M. The Influence of nonlinear mesoscale eddies on near-surface oceanic chlorophyll. *Science* **2011**, *334*, 328–332. [CrossRef]
57. Tan, D.P.; Hou, Y.Q.; Wang, C.Y.; Cheng, J.W.; Song, W.L. Analytical and experimental investigation of vibration response for the cracked fluid-filled thin cylindrical shell under transport condition. *Appl. Math. Model.* **2025**, *in press*.
58. Jovanović, A.; Pezo, M.; Pezo, L. DEM/CFD analysis of granular flow in static mixers. *Powder Technol.* **2014**, *266*, 240–248. [CrossRef]
59. Soto-Rivas, K.; Richter, D.; Escauriaza, C. Flow effects of finite-sized tidal turbine arrays in the Chacao Channel, Southern Chile. Renew. *Energy* **2022**, *195*, 637–647.
60. Qiu, Y.; Wang, F.N.; Zhang, Z.; Shi, K.Q.; Song, Y.; Lu, J.T.; Xu, M.J.; Qian, M.Y.; Zhang, W.A.; Wu, J.X.; et al. Quantitative softness and texture bimodal haptic sensors for robotic clinical feature identification and intelligent picking. *Sci. Adv.* **2024**, *10*, eadp0348. [CrossRef] [PubMed]
61. Li, L.; Xu, P.; Li, Q.H.; Zheng, R.Y.; Xu, X.M.; Wu, J.F.; He, B.Y.; Bao, J.J.; Tan, D.P. Particle flow modeling and ultrasonic vibration suppression method of microfluidic chip based on LBM-LES-DEM coupling. *Appl. Math. Model.* **2025**, *in press*.

62. Xin, Y.; Zhao, Y.; Zhang, T.C.; Zhang, F.S.; Yao, X.L.; Xiao, B.; Lin, P.; Qi, H.; Liu, S.F.; Tang, H.P. Multi-build orientation effects on microstructural evolution and mechanical behavior of truly as-built selective laser melting Ti6Al4V alloys. *J. Mater. Res. Technol.* **2024**, *30*, 3967–3976.
63. Ji, R.Q.; Shen, Q.T.; Zhang, L.; Zeng, X.; Qi, H. Novel photocatalysis-assisted mechanical polishing of laser cladding cobalt-based alloy using TiO_2 nanoparticles. *Powder Technol.* **2024**, *444*, 119990. [CrossRef]
64. Fu, D.N.; Sheng, J.; Wang, L.J.; Zhang, X.J.; Yang, R.D.; Li, X.K.; Wang, Y. In situ silver-loaded cellulose for high-strength antibacterial composite air filtration paper. *Cellulose* **2025**, *in press*.
65. Kan, K.; Zhang, Q.Y.; Xu, Z.; Zheng, Y.; Gao, Q.; Shen, L. Energy loss mechanism due to tip leakage flow of axial flow pump as turbine under various operating conditions. *Energy* **2022**, *250*, 124532. [CrossRef]
66. Hosseini, S.; Aghebatandish, S.; Dadvand, A.; Khoo, B.C. An immersed boundary-lattice Boltzmann method with multi relaxation time for solving flow-induced vibrations of an elastic vortex generator and its effect on heat transfer and mixing. *Chem. Eng. J.* **2021**, *405*, 126652. [CrossRef]
67. Lin, H.; Ma, M.; Qi, H.; Wang, X.; Xing, Z.; Alowasheeir, A.; Tang, H.; Jun, S.C.; Yamauchi, Y.; Liu, S.D. 3D-Printed photocatalysts for revolutionizing catalytic conversion of solar to chemical energy. *Prog. Mater. Sci.* **2025**, *151*, 101427. [CrossRef]
68. Chakraborty, I.; Biswas, G.; Ghoshdastidar, P.S. A coupled level-set and volume-of-fluid method for the buoyant rise of gas bubbles in liquids. *Int. J. Heat Mass Transf.* **2013**, *58*, 240–259. [CrossRef]